RESEARCH ARTICLE

Key Points:
- Global EPB occurrence analyzed throughout severe 17 March 2015 storm
- TIEGCM modeled observed transition of postsunset to postmidnight EPB activity
- Postmidnight EPBs initiated by storm time redistribution of ionospheric plasma

Correspondence to:
B. A. Carter,
brett.carter@rmit.edu.au

Global equatorial plasma bubble occurrence during the 2015 St. Patrick's Day storm

B. A. Carter[1,2], E. Yizengaw[1], R. Pradipta[1], J. M. Retterer[1], K. Groves[1], C. Valladares[1], R. Caton[3], C. Bridgwood[1], R. Norman[2], and K. Zhang[2]

[1]Institute for Scientific Research, Boston College, Boston, Massachusetts, USA, [2]SPACE Research Centre, RMIT University, Melbourne, Victoria, Australia, [3]Air Force Research Laboratory, Kirtland AFB, Albuquerque, New Mexico, USA

Abstract An analysis of the occurrence of equatorial plasma bubbles (EPBs) around the world during the 2015 St. Patrick's Day geomagnetic storm is presented. A network of 12 Global Positioning System receivers spanning from South America to Southeast Asia was used, in addition to colocated VHF receivers at three stations and four nearby ionosondes. The suppression of postsunset EPBs was observed across most longitudes over 2 days. The EPB observations were compared to calculations of the linear Rayleigh-Taylor growth rate using coupled thermosphere-ionosphere modeling, which successfully modeled the transition of favorable EPB growth from postsunset to postmidnight hours during the storm. The mechanisms behind the growth of postmidnight EPBs during this storm were investigated. While the latter stages of postmidnight EPB growth were found to be dominated by disturbance dynamo effects, the initial stages of postmidnight EPB growth close to local midnight were found to be controlled by the higher altitudes of the plasma (i.e., the gravity term). Modeling and observations revealed that during the storm the ionospheric plasma was redistributed to higher altitudes in the low-latitude region, which made the plasma more susceptible to Rayleigh-Taylor growth prior to the dominance of the disturbance dynamo in the eventual generation of postmidnight EPBs.

1. Introduction

Research on equatorial plasma bubbles (EPBs) has been driven in recent years by their negative influence on trans-ionospheric radio signals that are widely used for positioning, navigation, timing, and satellite communications [e.g., *Kelley et al.*, 2011, 2014, and references therein].

EPBs are widely understood to be caused by the Generalized Rayleigh-Taylor (R-T) plasma instability, in which a strong vertical plasma density gradient at the bottomside of the F layer and a strong upward plasma drift during the night combines to destabilize the plasma. The most recent formulation of the flux tube integrated R-T linear growth rate is given by *Sultan* [1996] as

$$\gamma_{RT} = \frac{\Sigma_P^F}{\Sigma_P^E + \Sigma_P^F} \left(V_p - U_L^P - \frac{g_e}{\nu_{eff}} \right) K^F - R_T,$$ (1)

where the first term V_p is the upward plasma drift speed, the second term U_L^P is the Pedersen conductivity-weighted neutral wind perpendicular to the magnetic field in the magnetic meridian plane, and the third term g_e/ν_{eff} is the altitude-corrected gravity divided by the flux tube integrated effective ion-neutral collision frequency, weighted by the electron density. These terms are multiplied by the flux tube integrated F (Σ_P^F) and E region (Σ_P^E) Pedersen conductivity ratio and K^F, which is the F region flux tube electron content height gradient (i.e., $1/N_e(\partial N_e/\partial h)$, where N_e is the flux tube electron content). Finally, R_T is the flux tube integrated recombination rate, which is assumed to be negligible in this analysis.

In the postsunset sector, the magnitude of the R-T linear growth rate in equation (1) is strongly dependent on the strength of the prereversal enhancement in the upward plasma drift V_p [e.g., *Heelis et al.*, 2012], which exhibits a strong longitudinal and seasonal dependence [e.g., *Abdu et al.*, 1981; *Tsunoda*, 1985; *Su et al.*, 2008; *Yizengaw et al.*, 2014]. The observed EPB climatology following decades of observations is well understood and can largely be explained by the longitudinal and seasonal variations in V_p [e.g., *Burke et al.*, 2004; *Su et al.*, 2008; *Carter et al.*, 2013]. Recent studies have employed global ionosphere-thermosphere models to successfully replicate the observed global EPB occurrence climatology [*Retterer and Gentile*, 2009; *Wu*, 2015].
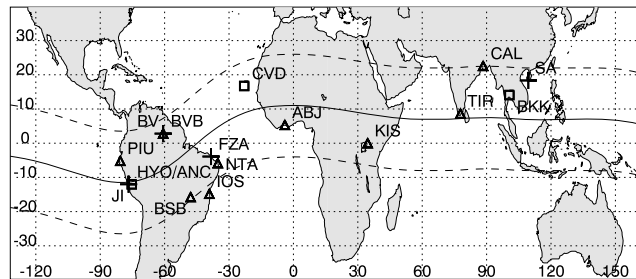
Figure 1. The locations of the radio receiver stations used in this analysis. Triangles indicate GPS receiver stations, squares indicate joint GPS and VHF receiver stations, and the crosses show the locations of nearby ionosondes. The solid line shows the location of the magnetic equator and the dashed lines show the ±15° magnetic latitudes.

The occurrence of EPBs during geomagnetic storms is further complicated by the existence of prompt penetration (under shielding) [e.g., *Basu et al.*, 2007, 2010; *Huang*, 2011], penetration (overshielding) [*Kikuchi et al.*, 2000, 2008], and disturbance dynamo [*Blanc and Richmond*, 1980] electric fields, which are all known to influence the vertical plasma drift that dominates the R-T linear growth rate [e.g., *Fejer et al.*, 1999; *Huang et al.*, 2001; *Kelley and Retterer*, 2008; *Abdu*, 2012, and references therein]. In some recent works, a global ionosphere-thermosphere model driven by geomagnetic activity has been shown to successfully reproduce the observed day-to-day EPB occurrence in the postsunset sector during peak EPB seasons [*Carter et al.*, 2014a, 2014b, 2014c]. In these analyses, small increases in the geomagnetic activity level were shown to be a significant driver in suppressing postsunset EPB growth at various locations with a delay of a few to several hours.

EPBs are also a common phenomenon in the postmidnight sector, and their occurrence is not that well understood. Quiet time postmidnight EPBs have been commonly observed during both the June and December solstices [e.g., *Li et al.*, 2011; *Gentile et al.*, 2011; *Nishioka et al.*, 2012; *Yizengaw et al.*, 2013], but they have also been known to occur during geomagnetic storms [e.g., *Fejer et al.*, 1999; *Palmroth et al.*, 2000; *Burke et al.*, 2009; *Gentile et al.*, 2011; *Abdu*, 2012]. The exact reasons as to why postmidnight EPBs occur outside of geomagnetic storms is still an ongoing issue [e.g., *Eccles*, 2004; *Burke et al.*, 2009; *Su et al.*, 2009; *de La Beaujardière et al.*, 2009; *Gentile et al.*, 2011; *Yizengaw et al.*, 2013]. However, postmidnight EPBs during geomagnetic storms are generally understood to be due to penetration electric fields [*Kikuchi et al.*, 2000, 2008] and/or the development of disturbance dynamo [*Blanc and Richmond*, 1980] electric fields, both of which cause upward plasma drifts, and thus promote EPB growth activity, in the postmidnight sector [e.g., *Fejer et al.*, 1999; *Palmroth et al.*, 2000; *Burke et al.*, 2009; *Gentile et al.*, 2011; *Abdu*, 2012].

In this study, a global network of Global Positioning System (GPS) and VHF receivers in addition to ionosondes are used to analyze the occurrence of EPBs before and during the 2015 St. Patrick's Day storm on 17 March. A global ionosphere-thermosphere model that is driven by geomagnetic activity inputs is used to calculate the R-T linear growth rate for the magnetic meridian of each station location throughout the period of this storm. The ionosphere-thermosphere model is then used as a tool to examine the physical phenomena that controlled EPB growth over this period.

2. Data Analysis and Modeling

The ionospheric scintillation measurements from GPS receivers from the Scintillation Network Decision Aid (SCINDA) [*Groves et al.*, 1997] and Low-latitude Ionospheric Sensor Network (LISN) [*Valladares and Chau*, 2012] networks were used, in addition to the Global Ionospheric Radio Observatory (GIRO) ionosonde [*Reinisch and Galkin*, 2011] network. Figure 1 shows the location of the SCINDA and LISN GPS and VHF stations used in this analysis, and a selection of nearby GIRO ionosonde stations, spanning the longitudes from South America to Southeast Asia and magnetic latitudes within ±15°. These stations are Piura (PIU), Huancayo/Ancon (HYO/ANC), Boa Vista (BVB), Brasilia (BSB), Ilheus (IOS), Natal (NTA), Cape Verde (CVD), Abidjan (ABJ), Maseno (KIS), Tirunelveli (TIR), Calcutta (CAL), and Bangkok (BKK). All stations have a dedicated GPS receiver that measures L band scintillations (using the minutely $S4$ index) due to ionospheric irregularities. Scintillation observations at VHF frequencies were also available at CVD, BKK, and HYO/ANC stations, and HYO/ANC, BVB, NTA, and BKK had the ionosonde stations JI, BV, FZA, and SA nearby, respectively.

The TIEGCM is a self-consistent time-dependent and physics-based three-dimensional model of the global thermosphere-ionosphere system [e.g., *Qian et al.*, 2014, and references therein]. In this study, the TIEGCM is used to calculate the R-T growth rate along the magnetic meridians of each of the stations in Figure 1 in the same manner as *Carter et al.*, 2014a [2014a, 2014c]. Variability in the TIEGCM, and the calculated growth rate, is induced by the solar and geomagnetic activity drivers of the model, the $F_{10.7}$ solar flux and the Kp index, respectively.

3. Results and Discussion

To understand how the St. Patrick's Day geomagnetic storm influenced the occurrence of EPBs, the GPS scintillation observations from all stations in Figure 1, in relation to their expected EPB climatologies, is analyzed. Figure 2 shows the local time versus date plots for each station, colored according to the 90th percentile of the $S4$ index ($S4_{90}$) measured by the GPS receivers within each hour. In the calculation of the hourly $S4_{90}$, all of the available satellite-to-ground links that recorded minutely $S4$ values were used. To exclude multipath effects, only GPS satellites above 30° elevation were considered. Also plotted is the maximum calculated R-T growth rate from the TIEGCM during 18–02 LT for each day in yellow. The Kp index is plotted in Figure 2m.

The GPS scintillation levels shown in Figure 2 exhibit different magnitudes between the stations. Overall, the strongest scintillations were observed by the South American stations that were close to ±15° magnetic latitudes, where the equatorial anomaly crests are typically expected. As revealed by several previous studies [e.g., *Burke et al.*, 2004; *Su et al.*, 2008; *Carter et al.*, 2013, and references therein], the EPB occurrence during March is expected to be relatively high across most longitude sectors. For the American sector, this period consists of a transition period from peak EPB occurrence during the December solstice to a minimum in the June solstice. Interestingly, the EPB occurrence, and the associated scintillation levels observed, in the Southeast Asian sector is significantly lower than the South American sector.

Throughout the period shown in Figure 2, GPS scintillations associated with EPBs were observed for most days in South America and Africa. This observation is expected and supports the well-known EPB climatology in these longitude sectors. Given that the growth of postsunset EPBs is favored at this time of the year by the close alignment of the day-night terminator and the local magnetic field, whether EPBs grow or not on any given day during this season is controlled by days when their growth is suppressed.

The Kp index in Figure 2m fluctuated between 0 and 4 prior to 17 March, when Kp reached a maximum of 8, followed by slow decline to prestorm levels. Outside of the main 17–18 March storm period, there is a noticeable anticorrelation between the Kp index and the calculated R-T growth rate; the most obvious example is the Kp increase to 4 on 7 March and the associated decrease in the R-T growth rate for all stations. This relationship was identified and investigated previously by *Carter et al.* [2014c] and *Carter et al.* [2014a], who found that these relatively small Kp variations were influencing the zonal neutral winds at the equator, and thus were influencing the strength of the prereversal enhancement in the upward plasma drift, and subsequently the R-T growth rate, after sunset.

Common to most stations in Africa and South America is a 2 day period, 17–18 March, when no scintillations (and therefore, no EPBs) were observed. The Indian stations observed EPBs on the first day of the storm, but none were observed for the following 2 days. The calculated R-T growth rate for each station's meridian is also shown to significantly decrease upon the commencement of the 17 March storm, and they each take approximately 2 days to recover to prestorm levels.

Figures 3a–3l show the time series of the GPS and VHF scintillation levels from 16 March to 21 March 2015. The dark gray shaded areas indicate local times (LT) between 18 and 02 (i.e., postsunset period) and the light gray shaded areas indicate 02–06 LT (i.e., postmidnight). The transition time from postsunset to postmidnight was defined as 02 LT, as it is clear in Figure 2 that scintillation commencing during postsunset hours sometimes continues until after 00 LT. Also plotted in Figures 3a–3l are the maximum calculated R-T growth rate in each station's magnetic meridian and the asterisks indicate the presence of spread F in nearby ionosonde data.

The presence of spread F was determined using an algorithm that counted the number of echoes detected from all frequency and range bins for each 15 min ionogram. Spread F was flagged for an ionogram when the total number of echoes exceeded a daily threshold value. To determine the daily threshold, we computed the daily statistical distribution of ionogram echo counts using multiple ionograms collected over a 24 h period, and the threshold was defined as 18 times the difference between the 20th and 10th percentiles, plus the
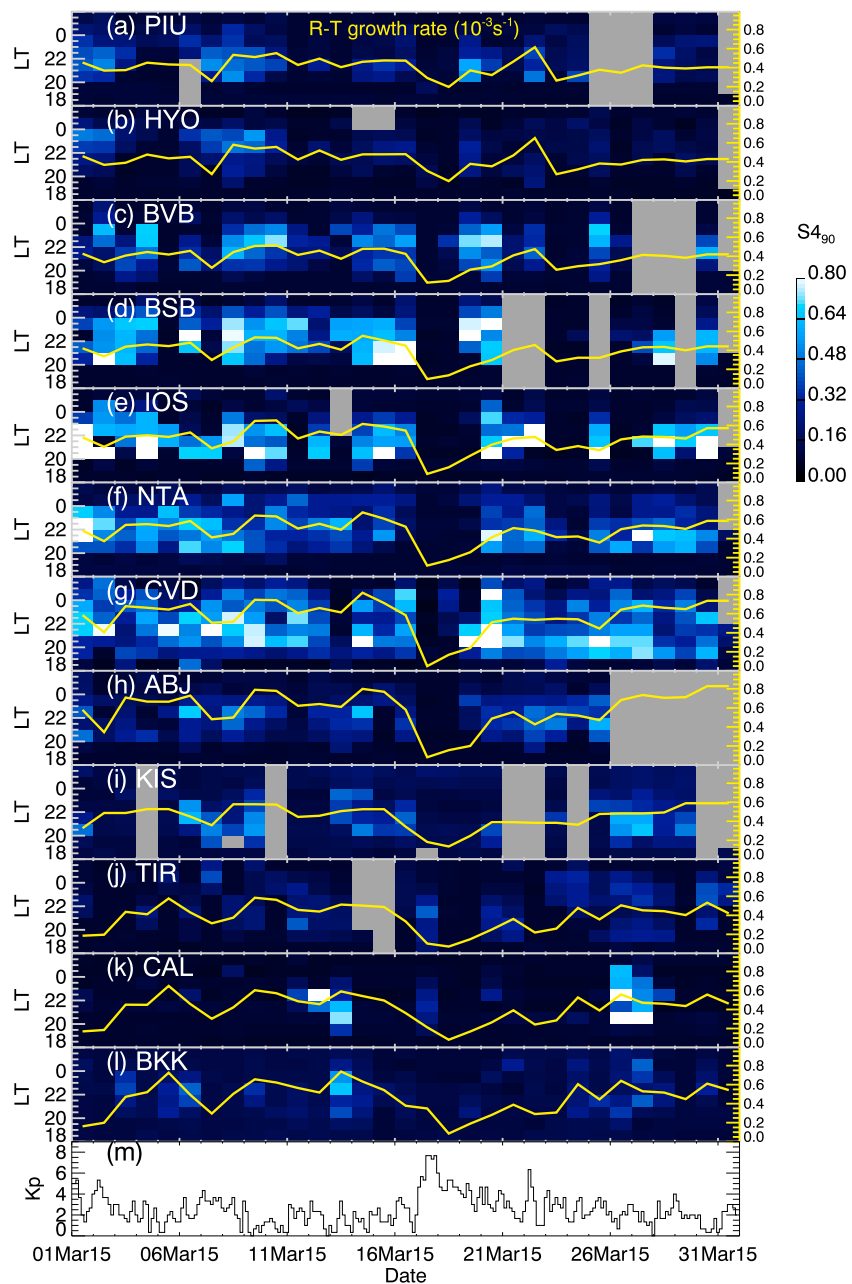
Figure 2. (a–l) Local time versus date throughout March 2015, colored according to the hourly $S4_{90}$ for all stations shown in Figure 1. Grey cells indicate data gaps. The yellow lines show the maximum calculated R-T growth rate from the TIEGCM between 18 and 02 LT and (m) the Kp index.

10th percentile in this daily distribution. As an example of how this spread *F* detection worked, Figure 4 shows a range-time-intensity-style plot of the number of echoes received from all frequency bins as a function of virtual height and time detected by the JI ionosonde during 17–18 March 2015. The spread *F* indicators are shown in the bottom panel, which are shown to correspond rather well to the occurrence of spread *F* in the ionosonde data.

From the data displayed in Figure 3 from March 16, it can be seen that the calculated R-T growth rate peaks early in the postsunset sector, just prior to the measured scintillation peak. The delay between these peaks is approximately 1–2 h, which is consistent with the typical amount of time for the EPBs to fully develop and cause L band scintillations [e.g., *Retterer*, 2010; *Carter et al.*, 2014b, 2014c]. For the stations that had both VHF and GPS scintillation observations, clear differences in the scintillation levels in the postsunset sector of 16
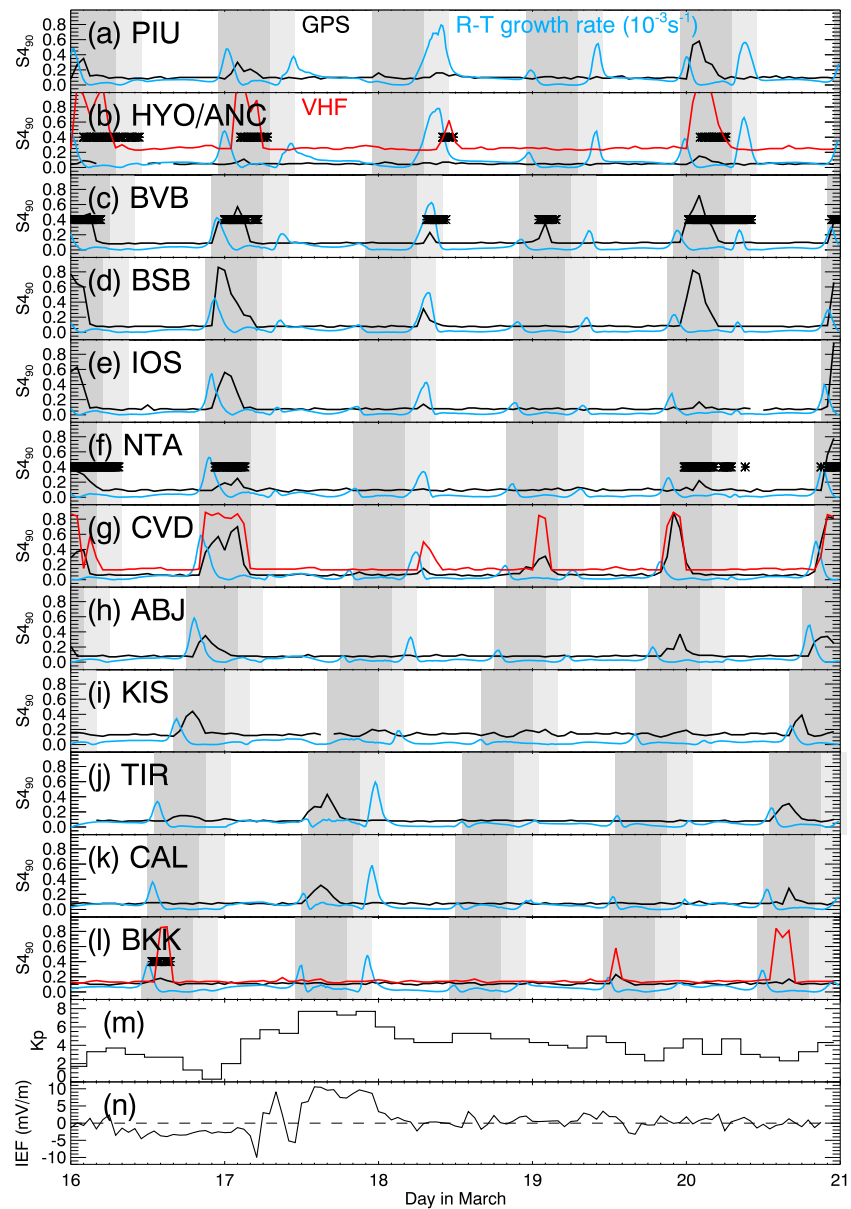
Figure 3. (a–l) The 90th percentile of the GPS $S4$ index as measured by the stations in Figure 1 in black over the period 16–21 March 2015. The red curves in Figures 3g and 3l are the 90th percentile of the VHF $S4$ index, and in 3b the hourly median $S4$ index is plotted in red, due to particularly noisy VHF $S4$ data from ANC. The asterisks indicate the presence of spread F detected at nearby ionosondes. The blue curves represent the maximum calculated R-T growth rate from the TIEGCM every 15 min. The dark gray shaded regions indicate 18–02 LT (i.e., the postsunset sector) and the light gray shaded regions indicate 02–06 LT (i.e., the postmidnight sector) for each station location. (m) The Kp index, for reference, and (n) the interplanetary electric field, propagated to the magnetopause.

March can be observed, particularly BKK. These differences are mostly attributed to the higher sensitivity of the lower frequency VHF waves to EPBs compared to GPS frequencies when background plasma densities are low [e.g., *Whalen*, 2009], in addition to the different satellite-link geometries. The VHF data from HYO/ANC is substantially noisier compared to those at BKK and CVD stations. As such, the hourly median of the HYO/ANC VHF $S4$ data was used and shows a good agreement with the spread F observations.

For GPS/VHF stations with nearby ionosondes, there is quite a good agreement between increased VHF/GPS scintillation activity and the detection of spread F. However, disagreements between scintillation and ionosonde data are noticeable in the early morning hours of 16 March at HYO/ACN and the postsunset hours of 19–20 March at BKK. The VHF link at HYO/ACN is directed toward the western sky, whereas the ionograms
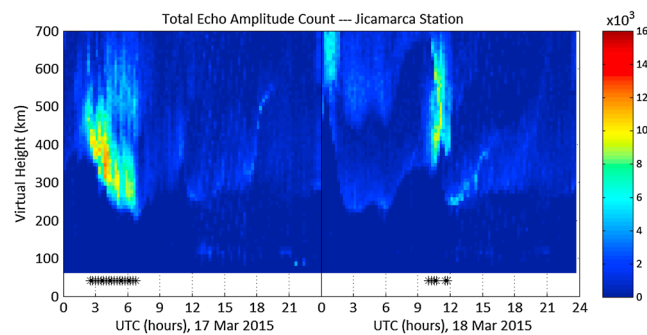
Figure 4. Range-time-intensity-style plot of ionospheric echoes received from JI ionosonde during 17–18 March 2015. Ionograms collected every 15 min were used in creating this plot. The color represents the accumulated number of echoes across all radio sounding frequencies. The asterisks below the figure indicate the presence of spread *F*, as discussed in the text.

from JI (not shown here) appear to indicate that the spread *F* was detected mostly from the eastern sky and the zenith. Figure 1 shows that BKK and the SAN ionosonde are separated by several hundred kilometers. Therefore, it appears that differences in scattering volumes are the likely cause of these apparent disagreements between these data.

It should be noted that for most stations, the calculated R-T growth rates exhibit a peak in the postsunset sector and not in the postmidnight sector on 16 March. The only exceptions to this rule are the stations in western South America, where a small R-T growth rate peak was calculated just prior to 06 LT, when no postmidnight scintillations were observed either at GPS or VHF frequencies.

On 17 March, the day of the commencement of the St. Patrick's Day storm, *Kp* rose to 8 at approximately the same time as local sunset for the Southeast Asian stations. Just prior to this *Kp* maximum, the interplanetary electric field (IEF) fluctuated between negative (Bz northward) and positive (Bz southward) and then remained positive for several hours during the storm's peak intensity. The change in IEF polarity from negative to positive just prior to the storm's peak at 12 UT coincides with the observation of postsunset EPBs by both Indian stations. It is interesting to note that neither BKK to the east, nor KIS to the west, observed EPBs, indicating that the source mechanism for the postsunset EPBs is confined in either longitude and/or local time. These observations are similar to those reported previously [e.g., *Basu et al.*, 2007, 2010; *Huang*, 2011] and can be explained by a prompt penetration electric field that is present for a short period of time and most effective in the postsunset local time sector, until a magnetospheric shielding electric field builds up to oppose it [*Kikuchi et al.*, 2000, 2008; *Abdu*, 2012]. The TIEGCM R-T growth rate did not increase for the Indian stations on 17 March, which is most likely due to the fact that the TIEGCM does not include a physically meaningful representation of prompt penetration electric fields [*Wang et al.*, 2008; *Zaka et al.*, 2010].

From KIS all the way to PIU in the west, no postsunset EPBs were observed on the night of 17 March. Further, the TIEGCM calculated R-T growth rates for these stations were significantly lower on 17 March compared to the same postsunset period on the day prior. This response of the modeled postsunset R-T growth rate to increased geomagnetic activity was highlighted by *Carter et al.* [2014a] to be due to disturbance dynamo effects. In Figure 3, the R-T growth rates reveal a peak in the postmidnight sector a few hours later, which is accompanied by a small but noticeable increase in the measured GPS scintillation level from CVD to PIU, excluding NTA. These small GHz scintillation increases are supported by available ionosonde and VHF scintillation data, which show the presence of EPBs above HYO/ACN and BVB stations, and strongly suggest that the lower GPS scintillation peaks observed by IOS and BSB are real EPBs. The background electron densities can be low in the postmidnight sector, which is most likely the cause of the lower GPS scintillation levels observed [*Whalen*, 2009], so the use of VHF scintillation and ionosonde spread *F* data are important for confirming the existence/absence of EPBs during these hours.

The differences in the background electron density between the stations is also the likely explanation for why the postmidnight GPS *S*4 peaks are observed to decrease from BSB (Figure 3d) in the east to PIU (Figure 3a) in the west, despite the relative increase in the calculated R-T growth rates. PIU and HYO/ACN are located closer to the magnetic equator where the equatorial anomaly trough is located, compared to BSB and BVB at higher latitudes where the equatorial anomaly crests are typically expected (Figure 1). Further, as pointed

out by *Carter et al.* [2014b], the nonlinearity of EPB development and the influence of background electron density on L band scintillations means that one should not necessarily expect a linear relationship between GPS $S4$ and the R-T growth rate.

Low background electron densities do not explain the lack of GPS scintillations detected by NTA in the post-midnight hours because the colocated ionosonde detected no spread *F*. The lack of EPB observations at NTA appears to be due to an unknown localized EPB suppression mechanism that the TIEGCM does not take into account; e.g., the daily variability in nonmigrating tides. On the other hand the VHF scintillation and the ionosonde spread *F* data confirm the existence of postmidnight EPBs at CVD, BVB, and HYO/ANC and are good indications that the lower GPS scintillation peaks observed by IOS and BSB are real EPBs.

While the TIEGCM appears to have successfully modeled the transition from postsunset EPBs during quiet time to postmidnight EPBs during the recovery phase of the storm for the stations between South America and Western Africa (excluding NTA), there are a few notable shortfalls of the TIEGCM revealed by this analysis.

For example, the effects of prompt penetration (or "under shielding") electric fields in generating EPBs in the Indian sector at the storm commencement are not noticeable in the modeled R-T growth rate. As previously mentioned, a physically meaningful inclusion of prompt penetration electric fields during southward inter-planetary magnetic field (IMF) turnings are required in order to capture these effects on EPB occurrence during the storm main phase.

The same can be stated about penetration (or "overshielding") electric fields during northward IMF turnings; i.e., the weakening of the IEF at $\sim$ 00 UT on 18 March, which coincided with the postsunset sector in South America and Western Africa and the postmidnight sector for Eastern Africa and Southeast Asia. The effect of this IEF decrease would have been a westward electric field and a subsequent decrease in the postsunset upward plasma drift (i.e., postsunset EPB suppression) and an increase in the postmidnight upward plasma drift (i.e., postmidnight EPB growth) [e.g., *Abdu*, 2012]. However, these effects are not explicitly included in the model. In reality, the IEF weakening at 00 UT on 18 March would have contributed toward the suppression of postsunset EPBs in the Western South American sector and enhanced EPB growth in the postmidnight sector in the Eastern African sector. However, these effects cannot be reliably separated from those of the disturbance dynamo [e.g., *Burke et al.*, 2009], which are included in the TIEGCM formulation. There is a noticeable increase in GPS scintillation measured by KIS during the transition from postsunset to postmidnight, but it is not clear whether this scintillation increase is due to EPBs in a low electron density environment or whether it is simply due to noise. Unfortunately, neither VHF nor ionosonde data were available to support KIS GPS scintillation observations in this study.

Finally, increased R-T growth rates were modeled for the Southeast Asian stations later that evening in the postmidnight sector, but no EPBs were observed. This inconsistency between model and observations suggests that the model is overestimating the equatorial velocity of the neutral wind disturbance caused by the increase in Joule heating in the auroral region and the onset/strength of the disturbance dynamo at the equator in this longitude sector. The increase in the R-T growth rate was calculated for all stations during this period, but the earliest postmidnight EPBs were observed by CVD 8 h after they were modeled to occur over Southeast Asia. This difference between model and observation is likely to be due to a difference in iono-spheric altitude in the Southeast Asian sector. Ion drag is a function of the ion-neutral collision frequency and therefore is proportional to the product of the electron and thermospheric densities. Thus, if the mod-eled ionosphere resides at a higher altitude than that observed, then the amount of ion drag experienced by the neutral wind disturbance will be less because of the significantly lower thermospheric density, resulting in a faster equatorward propagation velocity. The SA ionosonde station measurement of hmF_2 supports this explanation, which was measured to be $\sim$270 km compared to the TIEGCM hmF_2 output of $\sim$ 360 km at 18 UT on 17 March, not shown here.

With these model limitations noted, the fact that a self-consistent physics-based electrodynamics model of the global ionosphere-thermosphere system is capable of independently reproducing the observed EPB occurrence characteristics during the St. Patrick's Day storm across almost all of South America is an important result.

Significant scintillation activity was not observed on the night of 18 March, with the exception of CVD and BVB, both of which show a short interval of EPB activity during the postsunset sector. The postmidnight EPBs that were observed the night prior were not observed on this day. Interestingly, the calculated R-T

growth rates reflect less favorable EPB growth conditions in both postsunset and postmidnight periods on the evening of 18 March. The R-T growth rates for the western South American stations are still rather high in the postmidnight sector, but they are significantly less than at the same time on the day prior.

Finally, on the evening of 19 March, postsunset EPBs were observed at BKK, ABJ, CVD, and from BSB to PIU, and there is no indication of postmidnight EPBs. In terms of the calculated R-T growth rates, the postsunset peaks are rather small, but they are all larger compared to the previous day, which indicates that EPB growth is more favorable for all stations on the evening of 19 March.

The TIEGCM R-T growth rates presented in Figure 3 demonstrate that the TIEGCM is capable of modeling the global storm time dynamics that cause a transition of postsunset EPB activity on 1 day to postmidnight EPB activity on the next. In order to understand what exactly is happening within the R-T growth rate both before and during the St. Patrick's Day storm, an analysis was conducted of the three terms within the R-T growth rate for HYO/ANC, CVD, KIS, and BKK stations. Figures 5a–5d show the maximum calculated R-T growth rates over the same interval as Figure 3 for these stations. The first, second, and third R-T growth rate terms V_p, U_N, and g_e/v_{eff} are shown by the red, orange, and blue shaded areas, respectively.

The first feature from Figure 5 that is worth noting is that the second term U_N is always small compared to the first and third terms during the peak EPB growth periods. The postsunset growth periods along the magnetic meridians of these stations are initiated by an increase in the upward plasma drift; i.e., the postsunset prereversal enhancement. As the upward plasma drift term decreases, positive R-T growth is continued by an increased third term, which continues for a few more hours, even when the first term becomes negative.

In the postmidnight sector, the characteristics of the R-T growth period appear to be different in Figure 5. In particular, these postmidnight growth periods are shown to be initiated by an increased third term and then followed by an increase in the first term. This feature is most obvious for the CVD and HYO/ANC magnetic meridians in the morning of 18 March. It is clear from these plots that after the growth is initiated by the third term, the upward plasma drift term dominates the R-T growth rate in the postmidnight sector. As sunrise approaches, the R-T growth rates decrease abruptly, which is expected as the E region once again becomes populated via photoionization.

An interesting question that arises from the results in Figure 5b is what is the cause of the dominance of the third term in the R-T growth rate, prior to the upward plasma drift peak that later dominates the growth. To answer this question, Figures 5f and 5g show the apex altitude profiles of the flux tube integrated electron content above HYO/ANC at 5 UT (0 LT) and 7 UT (2 LT) on 17 and 18 March, respectively, as given by the TIEGCM. By comparing the apex altitude profiles from 5 UT on each day, it can be observed that the ionospheric plasma is higher in altitude on 18 March. This is also demonstrated by the F layer peak height, hmF_2 as indicated on the right. For reference, the hmF_2 observed by the JI ionosonde at these times is also shown in green.

Importantly, the slope of these profiles gives the vertical gradient in the flux tube integrated plasma density, which is proportional to K^F in the R-T growth rate, equation (1). The maximum slope of the electron content profiles is similar between 17 and 18 March at 0 LT (5 UT), but the altitude of the maximum slope is approximately 50 km higher on 18 March. This altitude difference is important because the strength of the third term significantly increases with altitude. From Figure 5a, it can be seen that at the moment of 0 LT on 18 March the plasma velocity is downward (i.e., negatively contributing to γ_{RT}). However, the R-T growth is still positive via the third term, g_e/v_{eff}, which is being amplified by the plasma density gradient at higher altitudes, K^F. Therefore, the positive R-T growth is initiated by the third term in the postmidnight hours, and not the first term, V_p, like in the postsunset sector.

Following the initial R-T growth caused by the ionospheric plasma at high altitudes close to 0 LT on 18 March, the vertical plasma drift turns from negative to positive, further enhancing the R-T growth for the next few hours. The difference in the upward plasma drift between 17 and 18 March can be clearly seen by the altitude changes in the plasma between 0 and 2 LT in Figures 5f and 5g.

The JI ionosonde data from 17 to 18 March displayed in Figure 4 can be compared to the modeling results from Figure 5a. In the postsunset hours on 17 March spread F was present for approximately 5 h, whereas on 18 March there was no detection of postsunset spread F. In the postmidnight of 18 March, however, spread F occurred for approximately 2 h following a rapid rise in altitude between 6 and 9 UT. This altitude rise between 6 UT and 9 UT was also modeled by the TIEGCM, as shown in Figure 5a. Importantly, the altitude of the F layer peak at 5 UT is ∼20 km higher on 18 March compared to 17 March; this can also be seen in
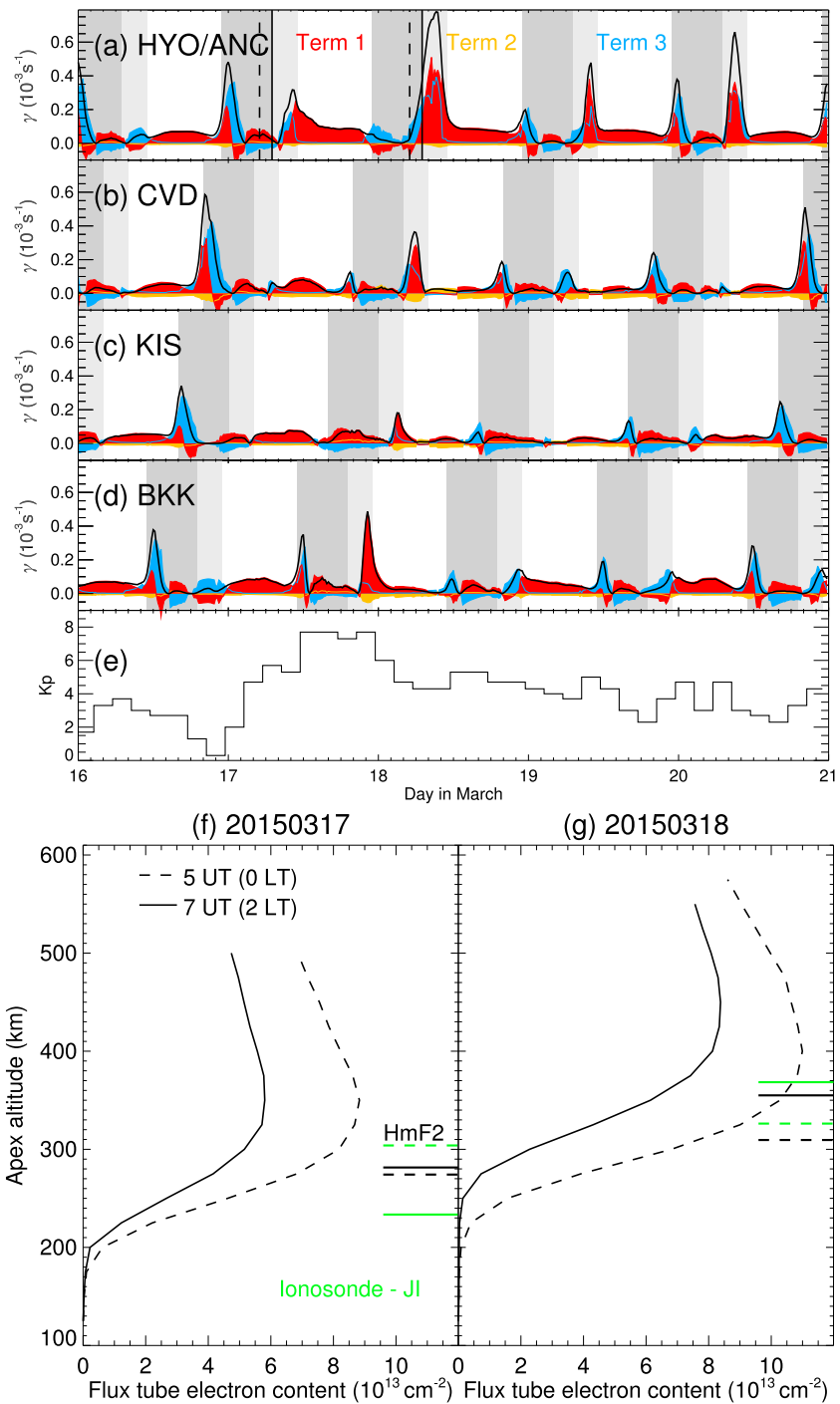
Figure 5. (a–d) The calculated R-T growth rate γ for HYO/ANC, CVD, KIS, and BKK throughout 16–21 March in black; i.e., the same as the blue curves in Figure 3. The red, blue, and orange shaded regions indicate the contributions to the R-T growth rate by the first (V_p), second (U_N), and third (g_e/ν_{eff}) terms, respectively. The dark gray shaded regions indicate 18-02 LT and the light gray shaded regions indicate 02-06 LT for each station. (e) The Kp index for reference. (f–g) Apex altitude profiles of the integrated electron content along the flux tubes above the magnetic equator in the same magnetic meridian as HYO/ANC from the TIEGCM. The black dashed and solid profiles represent the TIEGCM output from 5 UT to 7 UT, respectively, which are also indicated in Figure 5a. The horizontal lines on the right of each panel indicate the height of the F layer peak hmF_2 from the TIEGCM and the green horizontal lines are direct hmF_2 measurements from the JI ionosonde, also at 5 UT and 7 UT.

Figures 5f and 5g next to the model output of hmF_2. The model estimated this altitude increase to be ~40 km (i.e., double what was observed).

The profiles of the flux tube electron content determined using the TIEGCM, Figures 5f and 5g, revealed an increase in altitude of the maximum vertical gradient in the order of ~50 km at 5 UT between 17 and 18 March, which has resulted in a larger third term on 18 March, as shown in Figure 5a. Given the overestimation of the hmF_2 difference between 17 and 18 March by the TIEGCM, the altitude increase in the vertical flux tube electron content is also likely to be an overestimation. Despite this, the ionosonde observations show that the plasma was indeed at higher altitudes at the beginning of 18 March, which supports our finding that the R-T growth was initiated by a larger third term caused by a higher ionosphere compared to the previous day.

While the ionospheric plasma residing at higher altitudes in the early postmidnight sector initiated the postmidnight EPB growth, it is clear that the disturbance dynamo-driven upward plasma drift that followed some hours later was a dominant factor in continuing the R-T growth, and the subsequent EPBs that were observed.

One question that arises from this result is what causes this plasma redistribution to higher altitudes on 18 March compared to 17 March? It is possible that the higher altitude in the postmidnight sector could be a lingering effect of the plasma being driven to higher altitudes by the upward plasma drifts earlier during the daytime hours of 17 March. Although, another possible explanation is that the bottomside of the F layer is undergoing increased recombination due to increased concentration of molecular species on 18 March compared to 17 March, which effectively increases the height of the postmidnight plasma. Supporting this notion is the TIEGCM output of the O/N2 ratio, which shows a decrease of ~0.2 at 275 km altitude above HYO/ANC at 5 UT on 18 March compared to 17 March, not shown here. This decrease in O/N2, which is expected to be due to storm-induced heating and upwelling of N2, is small compared to the O/N2 decreases that cause so-called "negative ionospheric storms" in the middle latitudes [e.g., *Prölss*, 1992]. However, this O/N2 decrease can potentially explain the observed redistribution of the plasma to higher altitudes on 18 March, which has significant implications for R-T growth, as previously discussed.

From Figure 5, it is clear that the plasma redistribution during the severe geomagnetic storm on 17 March contributes toward the initial generation of postmidnight EPBs. While the significantly enhanced upward plasma drift in the early morning hours is a dominant factor in the growth of postmidnight EPBs, it has been made clear in this study that a redistribution of plasma to higher altitudes during the storm can initialize the postmidnight EPB growth via the R-T instability during the storm recovery phase.

Both disturbance dynamo and overshielding electric fields operate in the same direction, and as such previous studies have noted the difficulty in determining how much each electric field contributes toward the vertical plasma drift at the equator [e.g., *Burke et al.*, 2009]. The use of the TIEGCM as a tool in this study sheds some light on the source mechanism of the strong upward plasma drifts in the postmidnight sector. As the interface between the magnetosphere and ionosphere in the TIEGCM consists of only the high-latitude electric potential fields, it is clear that overshielding electric fields do not influence the R-T growth rate calculations in this analysis. As such, it is clear that the disturbance dynamo electric field is suppressing EPB growth in the postsunset sector and promoting EPB growth in the postmidnight sector for most stations in this analysis. The exception to this, of course, is the postsunset EPB occurrence on 17 March in the Indian sector, which was due to prompt penetration electric fields that are not explicitly included in the TIEGCM formulation. A recent study of the EPB activity over the Indian sector during this storm by *Singh et al.* [2015] investigates the influence of this prompt penetration electric field in detail. *Tulasi Ram et al.* [2016] recently explored the influence of enhanced magnetospheric electric fields at substorm onset [*Huang*, 2009, 2012] on the plasma over India for this storm, an effect that is also not considered in the TIEGCM formulation. It may be the case that overshielding electric fields also influence the vertical plasma drift, and consequently the EPB formation/suppression, but the IEF data in Figure 3n suggest that their role is short lived and small compared to the disturbance dynamo throughout the storm. As such, from this analysis it is clear that a large geomagnetic disturbance can generate a disturbance dynamo strong enough to suppress postsunset EPBs and promote postmidnight EPBs for multiple days across a wide range of longitudes, and when under shielding and overshielding electric fields are small.

4. Summary and Conclusions

An analysis of the occurrence of EPBs in the South American, African, and Southeast Asian longitude sectors during the 2015 St. Patrick's Day geomagnetic storm has been conducted. Following a burst of postsunset EPB activity over India at the beginning of the storm due to prompt penetration electric fields, EPB growth in the postsunset sector across most longitudes was suppressed for 2 days. Over the same period, EPB growth in the postmidnight sector was enhanced. Both the suppression of postsunset EPBs and the promotion of postmidnight EPBs was well described by the calculated R-T growth rate from the TIEGCM. Using a coupled thermosphere-ionosphere model allowed us to conclude that disturbance dynamo electric fields that took several hours to influence the equatorial region after the storm commencement were responsible for the suppression and growth of the postsunset and postmidnight EPBs, respectively. Further analysis of the post-midnight R-T growth rates revealed that the redistribution of plasma during the storm played a significant role in initiating the EPB growth, which was subsequently taken over by dynamo-driven upward plasma drift.

References

Abdu, M. A. (2012), Equatorial spread F/plasma bubble irregularities under storm time disturbance electric fields, *J. Atmos. Sol. Terr. Phys.*, 75–76, 44–56.

Abdu, M. A., J. A. Bittencourt, and I. S. Batista (1981), Magnetic declination control of the equatorial *F* region dynamo electric field development and spread F, *J. Geophys. Res.*, 86, 11,443–11,446.

Basu, S., S. Basu, F. J. Rich, K. M. Groves, E. MacKenzie, C. Coker, Y. Sahai, P. R. Fagundes, and F. Becker-Guedes (2007), Response of the equatorial ionosphere at dusk to penetration electric fields during intense magnetic storms, *J. Geophys. Res.*, 112, A08308, doi:10.1029/2006JA012192.

Basu, S., S. Basu, E. MacKenzie, C. Bridgwood, C. E. Valladares, K. M. Groves, and C. Carrano (2010), Specification of the occurrence of equatorial ionospheric scintillations during the main phase of large magnetic storms within solar cycle 23, *Radio Sci.*, 45, RS5009, doi:10.1029/2009RS004343.

Blanc, M., and A. Richmond (1980), The ionospheric disturbance dynamo, *J. Geophys. Res.*, 85, 1669–1686, doi:10.1029/JA085iA04p01669.

Burke, W. J., L. C. Gentile, C. Y. Huang, C. E. Valladres, and S. Y. Su (2004), Longitudinal variability of equatorial plasma bubbles observed by DMSP and ROCSAT-1, *J. Geophys. Res.*, 109, A12301, doi:10.1029/2004JA010583.

Burke, W. J., O. de La Beaujardière, L. C. Gentile, D. E. Hunton, R. F. Pfaff, P. A. Roddy, Y.-J. Su, and G. R. Wilson (2009), C/NOFS observations of plasma density and electric field irregularities at post-midnight local times, *Geophys. Res. Lett.*, 36, L00C09, doi:10.1029/2009GL038879.

Carter, B. A., K. Zhang, R. Norman, V. V. Kumar, and S. Kumar (2013), On the occurrence of equatorial *F*-region irregularities during solar minimum using radio occultation measurements, *J. Geophys. Res. Space Physics*, 118, 892–904, doi:10.1002/jgra.50089.

Carter, B. A., et al. (2014a), Geomagnetic control of equatorial plasma bubble activity modeled by the TIEGCM with *Kp*, *Geophys. Res. Lett.*, 41, 5331–5339, doi:10.1002/2014GL060953.

Carter, B. A., et al. (2014b), Using solar wind data to predict daily GPS scintillation occurrence in the African and Asian low-latitude regions, *Geophys. Res. Lett.*, 41, 8176–8184, doi:10.1002/2014GL062203.

Carter, B. A., E. Yizengaw, J. M. Retterer, M. Francis, M. Terkildsen, R. Marshall, R. Norman, and K. Zhang (2014c), An analysis of the quiet-time day-to-day variability in the formation of post-sunset equatorial plasma bubbles in the Southeast Asian region, *J. Geophys. Res. Space Physics*, 119, 3206–3223, doi:10.1002/2013JA019570.

de La Beaujardière, O., et al. (2009), C/NOFS observations of deep plasma depletions at dawn, *Geophys. Res. Lett.*, 36, L00C06, doi:10.1029/2009GL038884.

Eccles, J. V. (2004), The effect of gravity and pressure in the electrodynamics of the low-latitude ionosphere, *J. Geophys. Res.*, 109, A05304, doi:10.1029/2003JA010023.

Fejer, B. G., L. Scherliess, and E. R. de Paula (1999), Effects of the vertical plasma drift velocity on the generation and evolution of equatorial spread F, *J. Geophys. Res.*, 104, 19,859–19,869, doi:10.1029/1999JA900271.

Gentile, L. C., W. J. Burke, P. A. Roddy, J. M. Retterer, and R. T. Tsunoda (2011), Climatology of plasma density depletions observed by DMSP in the dawn sector, *J. Geophys. Res.*, 116, A03321, doi:10.1029/2010JA016176.

Groves, K. M., et al. (1997), Equatorial scintillation and systems support, *Radio Sci.*, 32, 2047–2064, doi:10.1029/97RS00836.

Heelis, R. A., G. Crowley, F. Rodrigues, A. Reynolds, R. Wilder, I. Azeem, and A. Maute (2012), The role of zonal winds in the production of a pre-reversal enhancement in the vertical ion drift in the low latitude ionosphere, *J. Geophys. Res.*, 117, A08308, doi:10.1029/2012JA017547.

Huang, C.-S. (2009), Eastward electric field enhancement and geomagnetic positive bay in the dayside low-latitude ionosphere caused by magnetospheric substorms during sawtooth events, *Geophys. Res. Lett.*, 36, L18102, doi:10.1029/2009GL040287.

Huang, C.-S. (2011), Occurrence of equatorial plasma bubbles during intense magnetic storms, *Int. J. Geophys.*, 2011, 401858, doi:10.1155/2011/401858.

Huang, C.-S. (2012), Statistical analysis of dayside equatorial ionospheric electric fields and electrojet currents produced by magnetospheric substorms during sawtooth events, *J. Geophys. Res.*, 117, A02316, doi:10.1029/2011JA017398.

Huang, C. Y., W. J. Burke, J. S. Machuzak, L. C. Gentile, and P. J. Sultan (2001), DMSP observations of equatorial plasma bubbles in the topside ionosphere near solar maximum, *J. Geophys. Res.*, 106, 8131–8142.

Kelley, M. C., and J. Retterer (2008), First successful prediction of a convective equatorial ionospheric storm using solar wind parameters, *Space Weather*, 8, S08003, doi:10.1029/2007SW000381.

Kelley, M. C., J. J. Makela, O. de La Beaujardiére, and J. Retterer (2011), Convective ionospheric storms: A review, *Rev. Geophys.*, 49, RG2003, doi:10.1029/2010RG000340.

Kelly, M. A., J. M. Comberiate, E. S. Miller, and L. J. Paxton (2014), Progress toward forecasting of space weather effects on UHF SATCOM after Operation Anaconda, *Space Weather*, 12, 601–611, doi:10.1002/2014SW001081.

Kikuchi, T., H. Lühr, K. Schlegel, H. Tachihara, M. Shinohara, and T.-I. Kitamura (2000), Penetration of auroral electric fields to the equator during a substorm, *J. Geophys. Res.*, 105, 23,251–23,261, doi:10.1029/2000JA900016.

Kikuchi, T., K. K. Hashimoto, and K. Nozaki (2008), Penetration of magnetospheric electric fields to the equator during a geomagnetic storm, *J. Geophys. Res.*, 113, A06214, doi:10.1029/2007JA012628.

Li, G., B. Ning, M. A. Abdu, X. Yue, L. Liu, W. Wan, and L. Hu (2011), On the occurrence of postmidnight equatorial *F* region irregularities during the June solstice, *J. Geophys. Res.*, *116*, A04318, doi:10.1029/2010JA016056.

Nishioka, M., Y. Otsuka, K. Shiogawa, T. Tsugawa, Effendy, P. Supnithi, T. Nagatsuma, and K. T. Murata (2012), On post-midnight field-aligned irregularities observed with a 30.8-MHz radar at low latitude: Comparison with *F*-layer altitude near the geomagnetic equator, *J. Geophys. Res.*, *117*, A08337, doi:10.1029/2012JA017692.

Palmroth, M., H. Laakso, B. G. Fejer, and R. F. Pfaff (2000), DE 2 observations of morningside and eveningside plasma density depletions in the equatorial ionosphere, *J. Geophys. Res.*, *105*(A8), 18,429–18,442, doi:10.1029/1999JA005090.

Prölss, G. W. (1992), Satellite mass spectrometer measurements of composition changes, *Adv. Space Res.*, *12*, 241–251, doi:10.1016/0273-1177(92)90473-B.

Qian, L., A. G. Burns, B. A. Emery, B. Foster, G. Lu, A. Maute, A. D. Richmond, R. G. Roble, S. C. Solomon, and W. Wang (2014), The NCAR TIE-GCM, in *Modeling the Ionosphere–Thermosphere System*, edited by J. Huba, R. Schunk, and G. Khazanov, pp. 73–83, John Wiley, Chichester, U. K., doi:10.1002/9781118704417.ch7.

Reinisch, B. W., and I. A. Galkin (2011), Global ionospheric radio observatory (GIRO), *Earth Planets Space*, *63*, 377–381, doi:10.5047/eps.2011.03.001.

Retterer, J. M. (2010), Forecasting low-latitude radio scintillation with 3-D ionospheric plume models: 1. Plume model, *J. Geophys. Res.*, *115*, A03306, doi:10.1029/2008JA013839.

Retterer, J. M., and L. C. Gentile (2009), Modeling the climatology of equatorial plasma bubbles observed by DMSP, *Radio Sci.*, *44*, RS0A31, doi:10.1029/2008RS004057.

Singh, R., S. Sripathi, S. Sreekumar, S. Banola, K. Emperumal, P. Tiwari, and S. Kumar (2015), Low latitude ionosphere response to super geomagnetic storm of 17/18 March 2015: Results from a chain of ground based observations over Indian sector, *J. Geophys. Res. Space Physics*, *120*, doi:10.1002/2015JA021509, in press.

Su, S.-Y., C. K. Chao, and C. H. Liu (2008), On monthly/seasonal/longitudinal variations of equatorial irregularity occurrences and their relationship with the postsunset vertical drift velocities, *J. Geophys. Res.*, *113*, A05307, doi:10.1029/2007JA012809.

Su, Y.-J., J. M. Retterer, O. de La Beaujardière, W. J. Burke, P. A. Roddy, R. F. Pfaff, G. R. Wilson, and D. E. Hunton (2009), Assimilative modeling of equatorial plasma depletions observed by C/NOFS, *Geophys. Res. Lett.*, *36*, L00C02, doi:10.1029/2009GL038946.

Sultan, P. J. (1996), Linear theory and modeling of the Rayleigh-Taylor instability leading to the occurrence of equatorial spread F, *J. Geophys. Res.*, *101*, 26,875–26,891.

Tsunoda, R. T. (1985), Control of the seasonal and longitudinal occurrence of equatorial scintillations by the longitudinal gradient in integrated *E* region Pedersen conductivity, *J. Geophys. Res.*, *90*, 447–456.

Tulasi Ram, S., et al. (2016), Duskside enhancement of equatorial zonal electric field response to convection electric fields during the St. Patrick's Day storm on 17 March 2015, *J. Geophys. Res. Space Physics*, *120*, doi:10.1002/2015JA021932, in press.

Valladares, C. E., and J. L. Chau (2012), The Low-Latitude Ionosphere Sensor Network: Initial results, *Radio Sci.*, *47*, RS0L17, doi:10.1029/2011RS004978.

Wang, W., J. Lei, A. G. Burns, M. Wiltberger, A. D. Richmond, S. C. Solomon, T. L. Killeen, E. R. Talaat, and D. N. Anderson (2008), Ionospheric electric field variations during a geomagnetic storm simulated by a coupled magnetosphere ionosphere thermosphere (CMIT) model, *Geophys. Res. Lett.*, *35*, L18105, doi:10.1029/2008GL035155.

Whalen, J. A. (2009), The linear dependence of GHz scintillation on electron density observed in the equatorial anomaly, *Ann. Geophys.*, *27*, 1755–1761, doi:10.5194/angeo-27-1755-2009.

Wu, Q. (2015), Longitudinal and seasonal variation of the equatorial flux tube integrated Rayleigh-Taylor instability growth rate, *J. Geophys. Res. Space Physics*, *120*, 7952–7957, doi:10.1002/2015JA021553-T.

Yizengaw, E., J. Retterer, E. E. Pacheco, P. Roddy, K. Groves, and R. C. P. Baki (2013), Postmidnight bubbles and scintillations in the quiet-time June solstice, *Geophys. Res. Lett.*, *40*, 5592–5597, doi:10.1002/2013GL058307.

Yizengaw, E., M. B. Moldwin, E. Zesta, C. M. Biouele, B. Damtie, A. Mebrahtu, B. Rabiu, C. F. Valladares, and R. Stoneback (2014), The longitudinal variability of equatorial electrojet and vertical drift velocity in the African and American sectors, *Ann. Geophys.*, *32*(3), 231–238, doi:10.5194/angeo-32-231-2014.

Zaka, K. Z., et al. (2010), Simulation of electric field and current during the 11 June 1993 disturbance dynamo event: Comparison with the observations, *J. Geophys. Res.*, *115*, A11307, doi:10.1029/2010JA015417.